PNAS RESEARCH ARTICLE | DEVELOPMENTAL BIOLOGY
APPLIED PHYSICAL SCIENCES

Gene expression detection in developing mouse tissue using in situ hybridization and μCT imaging

Vilma Väänänen[a,1], Mona M. Christensen[a], Heikki Suhonen[b], and Jukka Jernvall[a,c,1]

Edited by David Weitz, Harvard University, Cambridge, MA; received February 17, 2023; accepted May 7, 2023

High resolution and noninvasiveness have made soft-tissue X-ray microtomography (μCT) a widely applicable three-dimensional (3D) imaging method in studies of morphology and development. However, scarcity of molecular probes to visualize gene activity with μCT has remained a challenge. Here, we apply horseradish peroxidase–assisted reduction of silver and catalytic gold enhancement of the silver deposit to in situ hybridization in order to detect gene expression in developing tissues with μCT (here called GECT, gene expression CT). We show that GECT detects expression patterns of collagen type II alpha 1 and sonic hedgehog in developing mouse tissues comparably with an alkaline phosphatase–based detection method. After detection, expression patterns are visualized with laboratory μCT, demonstrating that GECT is compatible with varying levels of gene expression and varying sizes of expression regions. Additionally, we show that the method is compatible with prior phosphotungstic acid staining, a conventional contrast staining approach in μCT imaging of soft tissues. Overall, GECT is a method that can be integrated with existing laboratory routines to obtain spatially accurate 3D detection of gene expression.

μCT imaging | development | gene expression | in situ hybridization

Studies of animal morphology and development require accurate visual information of three-dimensional (3D) structures that are typically too opaque for visible-light imaging. X-ray imaging methods are highly suitable for this purpose due to their penetrance and high, uniform resolution. One of the currently most accessible formats of 3D X-ray imaging is X-ray microtomography (μCT), which allows microscale resolution imaging of intact samples with relatively straightforward sample preparation using benchtop-imaging equipment.

In X-ray attenuation μCT, X-ray projections of the sample are collected in various angles and then used to computationally generate a 3D model of how the sample reduces intensity of the X-rays traveling through it (1, 2). As the X-ray attenuation is considered proportional to the electron density and atomic number (Z) of the elements in imaged tissue, quantifiable volumetric data are obtained (1). 3D X-ray imaging techniques are readily applicable to nanoscale resolution imaging with techniques utilizing high-brightness synchrotron radiation, but nanoCT approaches without the need for synchrotron access are also currently available (2). High-resolution X-ray imaging techniques allow phase-contrast imaging, which has the practical benefit of samples not needing to go through any contrast enhancement procedures prior to imaging (1, 2).

Due to intrinsic low X-ray attenuation of soft tissue, attenuation-based μCT using polychromatic X-ray sources often requires procedures to increase contrast (1). This can be in some instances achieved by critical point drying (3), but more widely utilized method is the use of high-atomic number contrast agents (1, 4, 5).

Presence of the contrast agent in the tissue increases X-ray absorption of the sample in an energy-dependent manner (1, 2). At a given X-ray energy, the absorption coefficient μ depends on the atomic number Z roughly as $\mu \sim Z^4$, leading to that the X-ray absorption in heavier elements is much higher than that in lighter elements. This is exploited in many established X-ray imaging applications by using contrast agents that contain elements with high atomic number. Commonly used contrast agents include iodine ($Z = 53$) and tungsten (phosphotungstic acid, PTA, $Z = 74$), both recommended due to their ease of use and low toxicity (4, 6, 7). More recently, eosin, a common compound used in histology, was shown to generate high contrast suitable for high-resolution X-ray imaging of mouse kidneys (8). Bromine ($Z = 35$) present in eosin molecules generates X-ray attenuation during μCT imaging (8). Applying similar idea of utilizing conventional histological stains as μCT contrast agents, a method was described based on the use of hematein in complex with lead ($Z = 82$) for high-resolution nanoCT imaging of mouse livers and subsequent histological sectioning (9). Further developed method utilizing lead(III) acetate for nuclear staining currently allows for μCT imaging in aqueous solution and removal of the staining agent with ethylenediaminetetraacetic acid (10).

Significance

Accurate three-dimensional (3D) information about biological structures is necessary in studies of organ development and evolution. X-ray microtomography (μCT) has developed into a widely adopted 3D imaging method of hard and soft tissues, but merging μCT with methods to detect gene expression has remained a challenge. We show that enzymatic deposition of silver and enhancement of the silver deposit with gold can be utilized in conventional in situ hybridization to detect and visualize gene expression with μCT. The presented method is compatible with standard enzymatic in situ hybridization protocols and applicable both to unstained specimens and soft-tissue samples stained with phoshotungstic acid (PTA), allowing its easy implementation to already-existing pipelines of gene expression detection and μCT imaging.

Preprint servers: https://www.biorxiv.org/content/10.1101/2022.11.16.515587v2.

Author contributions: V.V., M.M.C., and J.J. designed research; V.V., M.M.C., and H.S. performed research; V.V. and J.J. analyzed data; and V.V. and J.J. wrote the paper.

The authors declare no competing interest.

This article is a PNAS Direct Submission.

[1]To whom correspondence may be addressed. Email: vilma.k.vaananen@helsinki.fi or jernvall@fastmail.fm.

This article contains supporting information online at https://www.pnas.org/lookup/suppl/doi:10.1073/pnas.2301876120/-/DCSupplemental.

Published June 6, 2023.

Yet another contrast agent is protargol, a silver–protein compound that has been used as a general tissue contrast stain in synchrotron μCT imaging of tooth development (11). Silver has atomic number 47, and in the energy range of 10 to 50 keV photons, it has absorption cross-section of more than 400 times higher per atom compared to carbon (12). Compared to conventional PTA staining, protargol enabled high-quality imaging of early-stage embryos, but suffered the same penetration problems as does PTA when imaging was extended to older whole-embryo heads and intact embryos (11).

In contrast to the imaging of tissues, a long-standing challenge in biological μCT imaging has been the limited number of methods available to detect specific molecules or gene activity (5). Quite recently, enhancement of metal 3,3-diaminobenzidine detection (nickel/cobalt DAB) with osmium tetroxide and uranyl acetate was used in the visualization of Ret antibody in wild-type and mutant mice (13). Enhanced DAB detection was also the basis of a method where use of peroxidase reporter gene enabled staining of specific cell populations in Drosophila legs and mouse brains (14). Also, a LacZ reporter gene system was recently established for μCT imaging of gene expression, utilizing the radiodensity of bromine in the product of the β-galactosidase reaction in dehydrated brain tissues (15).

Silver has demonstrated potential also as a more specific contrast stain for X-ray imaging. Recently, modified Fontana–Masson staining was used for 3D detection and quantification of melanin content in zebrafish larvae (16). Immunohistochemical approach by Metscher & Müller (17) utilized peroxidase-facilitated reduction of silver ions on sites of target proteins, and the 3D distribution of collagen type 2 and acetylated alpha tubulin in chick embryos was then visualized with μCT imaging. Immunohistochemical approach was also applied to visualize and quantify cultured cells and their nuclei inside tissue-engineering scaffolds (18).

Despite these advances, detection of gene expression, a central focus of developmental biology studies, remains challenging using μCT in a way that can be integrated with existing laboratory routines. To this end, here, we introduce a method for the detection of gene expression in messenger RNA (mRNA) level, utilizing peroxidase-assisted reduction of silver in in situ hybridization.

A Gene Expression CT (GECT) Method to Detect Gene Expression in Developing Tissues

To explore the usefulness of silver-based methods for visualization of gene expression using attenuation μCT, we detected the expression of two genes, *collagen type 2 alpha 1* (*Col2a1*) and *sonic hedgehog (Shh)*, in embryonic tissues of mice using silver-reducing in situ hybridization. We then compared the resulting expression patterns to conventional chromogenic in situ hybridization done in parallel with silver detection (Fig. 1 *A* and *B*).

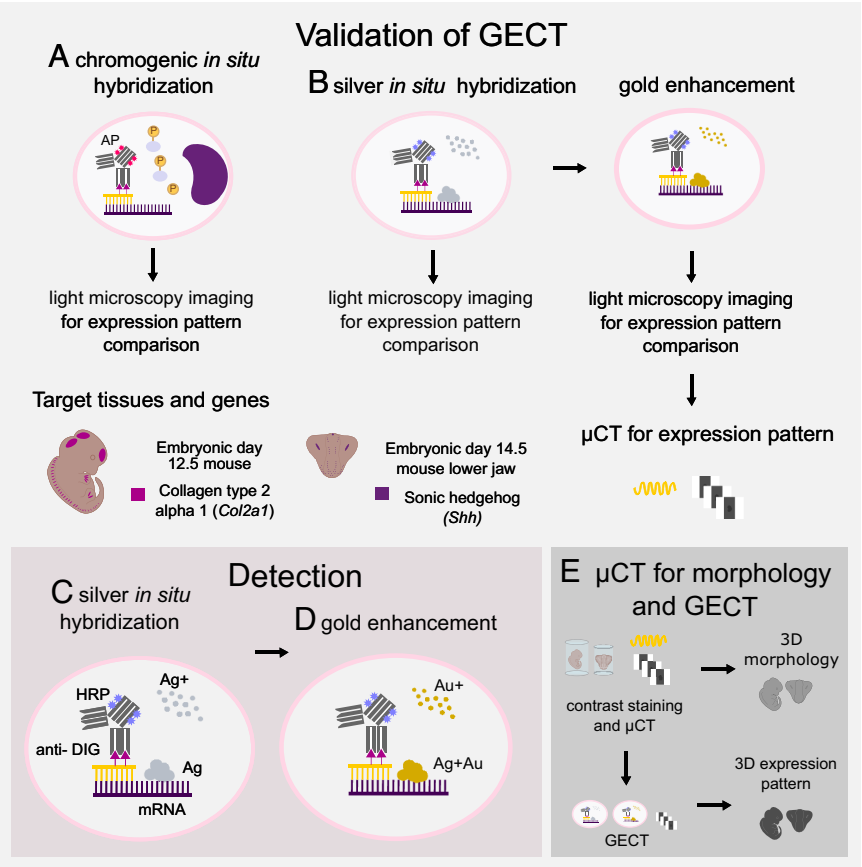

Fig 1. Validation of gene expression CT (GECT) and the pipeline for μCT imaging of morphology and gene expression. Validation was conducted by performing chromogenic (*A*) and silver (*B*) in situ hybridizations in parallel followed by gold enhancement on silver in situ samples. (*C*) Silver detection was conducted with horseradish peroxidase (HRP)–conjugated anti-DIG antibody and standard commercial detection kit (EnzMet, enzymatic metallography, Nanoprobes). During detection, HRP facilitates reduction of silver ions on sites of antibody (and probe) binding. (*D*) Gold enhancement (Gold Enhancement for LM, Nanoprobes) utilizes the silver condensates in the tissue as seeding particles and covers them with elemental gold by reducing gold ions in solution. The resulting signal was imaged with light microscopy and μCT. Some samples underwent μCT after silver in situ hybridization (*C*) and all samples underwent μCT after gold enhancement (*D*). (*E*) To further validate the detection scheme for routine use, we stained additional samples with PTA and imaged them with μCT to obtain representation of 3D morphology and conducted gene expression detection after μCT imaging for morphology.

In both in situ hybridization approaches, mRNA of interest is detected with digoxigenin (DIG)-labeled RNA-probes. Whereas in chromogenic in situ hybridization the detection is based on alkaline phosphatase (AP) activity, silver in situ hybridization utilizes anti-DIG antibody conjugated to horseradish peroxidase (HRP) (Fig. 1*C*). HRP facilitates specific reduction of silver ions in solution on sites of gene activity. In the presence of reducer, elemental silver condensates are formed (19, 20) (Fig. 1*C*).

Compared to proteins distributed abundantly, the general challenge in imaging gene expression is the detection of transient mRNA. Metscher and Müller showed that silver-reducing immunohistochemistry visualizes proteins when imaged with μCT (17). Here, our aim is to enhance the silver precipitate generated by peroxidase-assisted silver reduction with elemental gold ($Z = 79$), which has absorption cross-section of up to eight times higher than silver per atom in the energy range used in our imaging pipeline (12). To increase the X-ray absorption of the expression sites, we utilized a commercial gold enhancement kit (Nanoprobes) to strengthen the expression signal and compared the resulting expression patterns to the conventional chromogenic method (Fig. 1*D*).

Gold enhancement is based on autometallography, where metal ions are catalytically reduced to elemental metal on the surface of already-existing metal particles in the presence of a reducer (21, 22). Commercial gold enhancement protocols are patented and do not state exact components of the detection reaction (23, 24). Gold enhancement kit contains a set of solutions called "enhancer," "activator," "initiator," and buffer (23, 24), whereas conventional autometallographic silver enhancement is usually performed with some source of silver ions (silver acetate, silver lactate) and a reducer (usually hydroquinone), paired with a colloid that decelerates the reaction and a suitable buffer (25). Sodium thiosulfate washes reduce the background staining and stop the detection reaction (23, 25).

To test whether our approach can detect widespread expression fairly deep inside the tissue, we conducted in situ hybridization for *Col2a1* in embryonic day 12.5 mouse embryo (Fig. 1). This should provide largely comparable patterns to the type II collagen protein detected in embryonic chicken previously using μCT (17).

During later embryogenesis after embryonic day 12, *Col2a1* is a prominent marker of differentiating chondrocytes in the developing skeletal system (26–28). More specifically, *Col2a1* is highly expressed in developing digits and limbs, developing vertebrae and ribs, and developing parietal and occipital bones of the skull (29).

To challenge the method in conditions where the target molecule is expressed locally and in low numbers, we show that GECT can be used to visualize the expression of *Shh* in a developing tooth germ of embryonic mouse (Fig. 1). *Shh* is a central gene in the development of several mammalian organ systems, including ectodermal appendages such as teeth, hair buds, and taste buds (30–32). During mouse embryonic day 14 to 15, *Shh* is expressed in the embryonic signaling center of a tooth germ, called the primary enamel knot (33–35).

To further establish the method as a way to visualize 3D gene expression and tissue morphology from an individual tissue sample, we combine phosphotungstic acid staining and μCT imaging of 3D morphology to the detection pipeline, from now on called GECT (Fig. 1*E*).

Results

For the detection of an abundantly expressed gene, we tested silver in situ hybridization and gold enhancement for *Col2a1* in embryonic day 12.5 mice. Chromogenic detection of *Col2a1* (Fig. 2*A*, n = 2) is consistent with silver detection and gold enhancement (Fig. 2 *B* and *C*, n = 2), showing expression in developing cartilage of limbs, spine, and skull. Chromogenic detection converts 5-bromo-4-chloro-3-indolyl-phosphate to 5,5′-dibromo-4,4′-dichloro-indigo with alkaline phosphatase activity (36). We briefly examined whether alkaline phosphatase substrate would provide X-ray contrast for expression regions in our samples imaged in liquid medium, as contrast is described by Ermakova et al. 2021 (15) in dehydrated brain tissue with conversion of 5-Bromo-4-chloro-1*H*-indol-3-yl β-D-galactopyranoside to 5,5′-dibromo-4,4′-dichloro-indigo. We were not able to produce a signal for *Col2a1* expression with alkaline phosphatase–based method (*SI Appendix*, Fig. S1).

Combination of gold and silver in the detection of *Col2a1* enables visualization of expression via μCT (Fig. 2*D*).

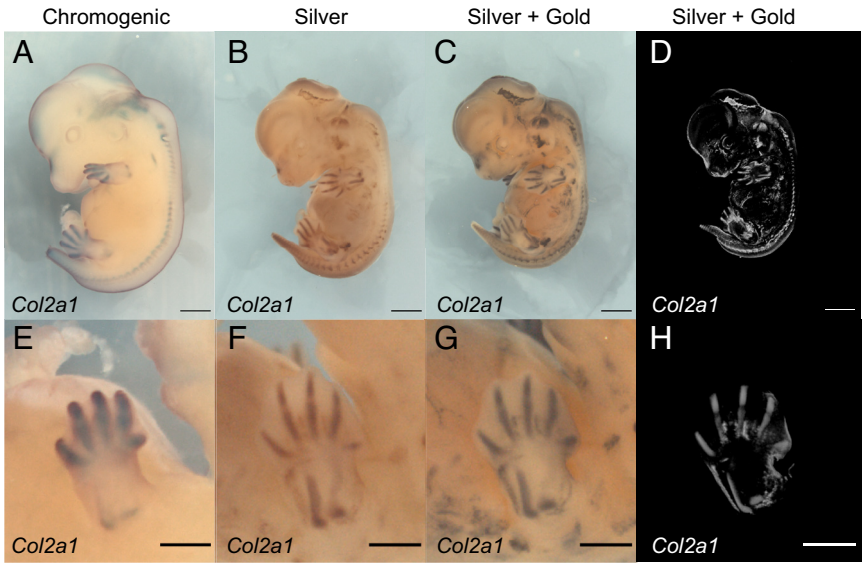

Fig 2. Detection of *Collagen type 2 alpha 1 (Col2a1)* expression with μCT. (*A*) Chromogenic in situ hybridization of *Col2a1* in e12.5 mouse embryo. (*B*) Silver in situ hybridization of *Col2a1*. (*C*) Gold enhancement of silver in situ hybridization shown in *B*. (*D*) Volume rendering of *Col2a1* expression shown in *C*. (*E*) Close-up of the *Left Upper* limb shown in *A*. (*F*) Close-up of the *Left Upper* limb shown in *B*. (*G*) Close-up of the *Left Upper* limb shown in *C*. (*H*) Close-up of the *Left Upper* limb shown in *D*. (Scale 1,000 μm in *A–D*, 500 μm in *E–H*.)

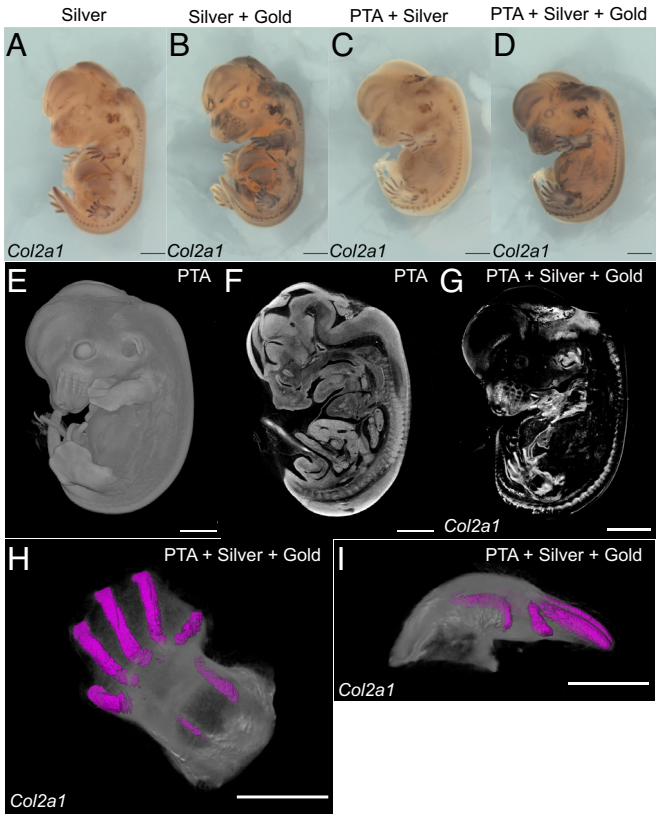

Fig 3. Tissue contrast staining before gene expression detection. (*A*) Silver in situ hybridization of *Col2a1* without prior PTA stain. (*B*) Gold enhancement of *Col2a1* detection shown in *A*. (*C*) Silver in situ hybridization of *Col2a1* in the mouse embryo stained with PTA. (*D*) Gold enhancement of *Col2a1* detection shown in *C*. (*E*) Volume rendering of the contrast-stained mouse embryo, prior to in situ hybridization. (*F*) Cross-section of the mouse embryo shown in *E*. (*G*) Volume rendering of *Col2a1* expression shown in *D*. (*H*) Close-up of the *Left* hindlimb shown in *G*. Segmented *Col2a1* expression inside the limb shown in magenta, sagittal view. (*I*) Segmented *Col2a1* expression (magenta) inside the *Left* hindlimb, transverse view. (Scale 1,000 μm in *A*–*G*, 500 μm in *H*–*I*.)

Expression of *Col2a1* is particularly clear in limbs of the developing embryo, as shown in the upper limb in Fig. 2 *E*–*H*. The silver in situ hybridization and gold enhancement generate a clear-cut signal, from which interphalangeal joint spaces are distinguishable as nonexpressing tissue (Fig. 2 *F*–*H*), also visible in Movie S1.

To test visualization of both the tissue morphology and the gene expression in the same sample, we applied silver in situ hybridization and gold enhancement to samples that had undergone phosphotungstic acid (PTA) staining and μCT imaging for morphology. Compared to control samples without PTA staining prior to in situ hybridization (Fig. 3 *A* and *B*, n = 2), PTA-stained samples replicated the expected expression pattern of *Col2a1* in both stages of detection (Fig. 3 *C* and *D*), similarly with slight increase in background when gold enhancement was applied. μCT reconstruction of the PTA-stained sample prior to in situ hybridization shows good contrast between the sample and the scanning medium (Fig. 3*E*) and between tissue compartments (Fig. 3*F*). Gold-enhanced signal of *Col2a1* expression from the same sample was detectable with μCT (Fig. 3*G*), and segmented expression regions inside the hindlimb are shown in Fig. 3 *H* and *I*.

To focus on locally and transiently expressed developmental genes, we examined *Shh* expression in developing mouse lower jaws. In the embryonic day 14 lower jaw samples including tongue, *Shh* expression is detected with chromogenic in situ hybridization in enamel knots of the molars, hair and whisker buds of the chin, and taste papillae of the tongue (Fig. 4*A*, n = 2). Silver in situ hybridization replicates this pattern (Fig. 4*B*, n = 3) and gold enhancement of the silver detection preserves it (Fig. 4*C*, n = 3). We also compared chromogenic and silver in situ hybridization on histological sections (*SI Appendix*). Silver in situ hybridization performed equally to chromogenic detection in every trial (*SI Appendix*, Table S1). We also observed that *Shh* expression regions detected with silver in situ hybridization and gold enhancement are more spatially defined upon visual inspection compared to the signal produced by chromogenic detection (Fig. 4 *A*–*C*, see also *SI Appendix*, Fig. S2 visualizing slide in situ hybridization for *Shh*).

μCT imaging of jaw samples was conducted after both silver in situ hybridization and gold enhancement. μCT imaging of silver detection resulted in no observable attenuation on sites of *Shh* expression and imaging after first gold enhancement round visualized expression regions only partially (*SI Appendix*, Fig. S3). In samples containing the tongue, all expression sites were visible with μCT after repeating gold enhancement (Fig. 4 *D*–*F*, *Shh* in enamel knot shown in teal color).

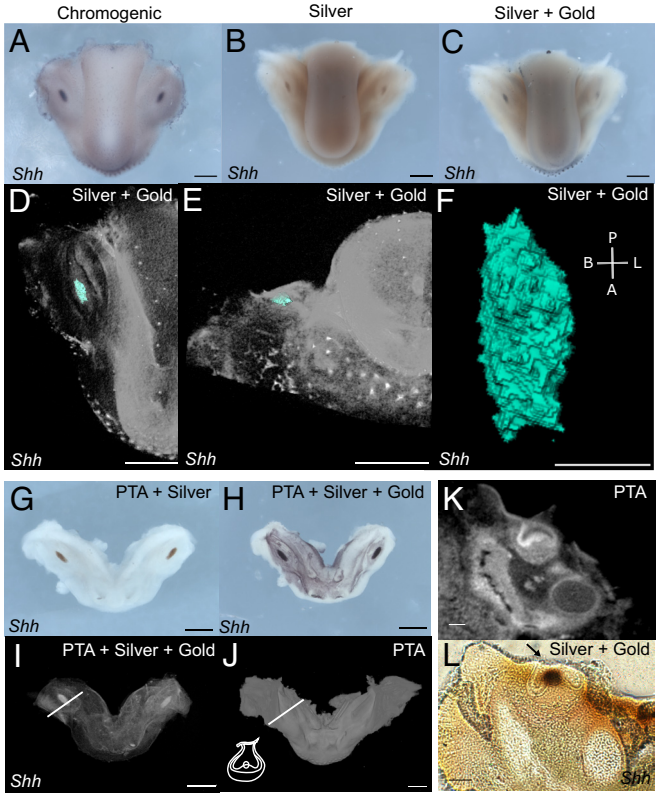

Fig 4. μCT visualization of *Sonic hedgehog (Shh)* expression from unstained and contrast-stained tissues**.** (*A*) Chromogenic in situ hybridization of *Shh* expression in mouse e14.5 jaw. (*B*) Silver in situ hybridization of *Shh*. (*C*) Gold enhancement of *Shh* detection shown in *B*. (*D*) Volume rendering of *Shh* expression from μCT data, occlusal view. Expression in the embryonic molar shown in teal. (*E*) Volume rendering of *Shh* expression, expression in the embryonic molar shown in teal, frontal view. (*F*) Segmented expression region of *Shh* in the mouse molar, occlusal view. B = buccal, L = lingual, A = anterior, P = posterior. (*G*) Silver in situ hybridization for *Shh* applied to contrast-stained jaw. (*H*) Gold enhancement of *Shh* detection shown in *G*. (*I*) Volume rendering of μCT data from the jaw shown in *H*. (*J*) Volume rendering of contrast-stained jaw shown in *G*–*I*, prior to *Shh* detection. White line shows approximate section plane shown in *K*. Structures of a developing molar in shown plane are visualized in schematic in the lower left corner. (*K*) Frontal virtual section of a developing molar stained with PTA. (*L*) Frontal vibratome section of the jaw underwent silver in situ hybridization and gold enhancement for *Shh* (dark brown). Epithelial tearing shown with arrow. (Scale 500 μm in *A*–*E*, 100 μm in *F*, 500 μm in *G*–*J*, 100 μm in *K*–*L*.)

Similar to the *Col2a1*, *Shh* expression was detectable in the tissues stained with PTA (Fig. 4 *G* and *H*, n = 2) and visible in μCT (Fig. 4*I*, n = 2). We note that whereas PTA staining before in situ hybridization provided contrast for μCT detection of jaw tissue (Fig. 4 *J* and *K*), PTA is washed away from tissues during in situ hybridization (Fig. 4*I*).

In situ hybridization treatments cause tissue distortion, which may affect 3D reconstructions. When compared to frontal virtual section of a developing molar from jaw stained with PTA and imaged with μCT (Fig. 4*K*), frontal vibratome section of a whole-mount sample undergone in situ hybridization and gold enhancement shows tearing of the surface epithelium on the site of the dental chord (arrow, Fig. 4*L*). The expression region of *Shh* in whole-mount samples (Fig. 4*L*) is consistent with section in situ hybridization (*SI Appendix*, Fig. S2). Epithelial tearing occurred frequently in jaw samples and also in samples undergone chromogenic detection, and is thus not specific to the steps of gold enhancement. We observed no drastic tearing or distortion of tissues in whole-embryo samples on the sites of expression. Control sample without prior PTA staining shown in Fig. 3 *A* and *B* exhibits the extent of tearing in the stomach region that occurred during *Col2a1* detection. Samples stained with PTA prior to detection show slightly less tissue tearing (Fig. 3 *C* and *D*).

Discussion

Despite the wide range of resolution available in μCT imaging, there remains the challenge to image specific molecules or gene activity. Initially, peroxidase-assisted reduction of silver was used to visualize the distribution of collagen type II and acetylated alpha-tubulin proteins in chick embryos (17). This approach utilized conventional immunohistochemical detection of proteins, in which antibody is conjugated with HRP (20). Here, we apply a similar, straightforward approach to detect and visualize mRNA distribution in whole-mount samples.

In addition to the lack of molecular markers, contrast agent use and development for μCT imaging is still regarded to be in its early stages compared to other imaging modalities (2, 5). Other 3D imaging techniques such as light sheet microscopy have already benefitted from parallel development of optics, tissue-clearing approaches, and fluorophore design, allowing simultaneous detection of multiple genes. Some animal models allow high-resolution imaging of even fairly large specimens (37). While being isotropic, the resolution of μCT imaging is limited by the X-ray spot size and is usually below the achievable resolution of light-sheet microscopy approaches. Nevertheless, in many instances, the practical resolution of μCT still reaches ten to tens of microns (38), which remains morphologically relevant while being able to routinely image whole organisms. When the structure of the sample is variable or otherwise problematic for imaging of fluorescent signals (for example, when animal is opaque and not suitable for tissue clearing), μCT tends to generate 3D data that are uniform in quality.

Here, our aim was to develop a method that can be incorporated into the existing pipelines of i) μCT imaging of soft tissue and ii) detection of gene expression with in situ hybridization. We show that the commonly used phosphotungstic acid staining can be performed prior to GECT. With two rounds of μCT imaging, it will be possible to obtain first the tissue structure and then, after the in situ hybridization, gene expression pattern in 3D.

In situ hybridization is a robust, widely used method for spatial detection of gene expression, and there exists a variety of optimized protocols for a range of model organisms and both for tissue sections and whole-mount samples (39–45). The pipeline presented here requires relatively small changes to the existing in situ hybridization pipelines. Compared to the commonly used chromogenic detection of gene expression patterns, silver in situ hybridization provides more visually precise spatial readout of gene expression [Figs. 2 and 4 and *SI Appendix*, Fig. S1 (20)]. An added advantage is that if μCT imaging is not required, the pipeline can be stopped after the silver detection and the samples can be sectioned for histological analyses.

Areas benefitting from further developments include tissue distortion caused by in situ hybridization. Whereas in developing mouse molars there is tearing of epithelium after in situ hybridization, whole-mouse embryos hold their shape better, exhibiting only a slight tearing in the stomach. It is conceivable that these are not caused by any distinct step in the protocol but stem from repeated processing of the samples. One easily modifiable aspect would be the length and number of dehydration and rehydration steps preceding μCT and in situ hybridization. Time required for sample collection, tissue staining, μCT imaging of morphology, in situ hybridization, and μCT imaging of gene expression presented in this proof-of-concept work is approximately 2 wk and it has room for further developments. Based on different responses of the samples we used, we additionally suggest that distortion is somewhat dependent on sample size and type. Specific knowledge of the target tissue allows further optimization of the detection conditions.

We observed modest superficial background signal in the samples with silver detection, consistent with the observations of Metscher & Müller (17). This background became stronger alongside the expression signal when the same samples were processed through gold enhancement (Figs. 2–4). The benefit of μCT imaging in this context is also that the signal visible on the surface of the sample can be discriminated from the signal within the sample. Nevertheless, we recommend that at least when working with unfamiliar probes and genes known to have superficial expression, one should run chromogenic detection alongside the combination of silver and gold detection to be able to distinguish the background from the signal.

Metscher and Müller propose a quantification method for the level of gene expression based on the intensity values of μCT imaging data (17). We note that silver in situ hybridization is an enzyme-based detection method and inherently includes variation in the intensity of the signal not necessarily reflecting the biological state of the tissue. Gold enhancement is not based on enzymatic activity and seems to replicate the signal of silver detection faithfully, and it remains to be explored how well the method captures differences in gene expression levels.

In conclusion, the protocol developed in this study should help to integrate μCT imaging and detection of gene expression using in situ hybridization, two commonly used methods that, when combined, should broaden opportunities for biological imaging.

Materials and Methods

Ethics Statement. All animal work was performed in accordance with the guidelines of the Finnish Authorization Board under licenses KEK16-021 and KEK19-019.

Animal Work. Wild-type HsdWin:NMRI mice (Naval Medical Research Institute, Envigo) were used for collection of tissue samples. Embryonic age was determined as days from the appearance of the vaginal plug (day 0). Embryos were fixed overnight using 4% paraformaldehyde (PFA) in 1× phosphate-buffered saline (1× PBS), +4 °C. Lower jaws were dissected in Dulbecco's phosphate-buffered saline under a light microscope before overnight fixation with 4% PFA in +4 °C. Samples were dehydrated via methanol series and stored in 100% methanol at −20 °C.

Phosphotungstic Acid Staining. Samples were rehydrated from 100% MeOH to 70% EtOH and stained with 0.3% phosphotungstic acid (PTA) (P4006-100G, Sigma-Aldrich, Saint Louis, Missouri, USA) in 70% EtOH for 24 to 48 h at +8 °C (7). After staining, the samples were returned to 70% EtOH. X-ray imaging of PTA-stained samples was conducted in 70% EtOH using 1.6 mL polypropylene tubes with screw cap and seal (CryoPure, Sarstedt, Nümbrecht, Germany). The samples were stored 70% EtOH at +4 °C until proceeding with in situ hybridization.

Probe Synthesis. Plasmid construct (Bluescript SK-, Stratagene, San Diego, California, USA) for mouse (*Mus musculus*) *Col2a1* RNA probes (405 bp) was generated according to Metsäranta et al. (46) and provided by Mikkola lab, Institute of Biotechnology. RNA probes specific to mouse (*Mus musculus*) *Shh* gene exons 1, 2, and 3 were generated using the following primers: CGTAAGTCCTTCACCAGCTTG (forward) and GCTGACCCCTTTAGCCTACA (reverse). cDNA was prepared from mouse embryonic molar tooth RNA (extracted using RNeasy Plus Micro kit, Qiagen, Düsseldorf, Germany) and cDNA constructs were inserted in TOPO II PCR-plasmids using TOPO TA Cloning kit with chemically competent cells according to manufacturer's protocol (Thermo Fisher Scientific, Waltham, Massachusetts, USA). Prior to in vitro RNA synthesis, plasmids were extracted using Miniprep kit (Qiagen, Düsseldorf, Germany).

Plasmids were linearized and probes were prepared as described by Wilkinson & Nieto (47) using DIG-conjugated nucleotides (Roche, Basel, Switzerland). Specificity of target mRNA binding was confirmed using a sense probe in slide in situ hybridization and in whole-mount in situ hybridization, and both chromogenic and metallographic detections were used.

Whole-Mount In Situ Hybridization. Steps were conducted in a 24-well plate (Cellstar, Greiner Bio-One, Kremsmünster, Austria) in a volume of 900 µL unless otherwise stated. Samples stored in 100% methanol were rehydrated to 1x PBS-T [1× PBS with 0.1% Tween20 (P7949-500ML, Sigma-Aldrich, Saint Louis, Missouri, USA)] through a descending methanol series. Ethanol series was used for samples that had been stained with phosphotungstic acid and imaged with µCT prior to in situ hybridization. After three 15-min washes in 1× PBS-T, the samples were incubated in 3% hydrogen peroxide (95299-2.5L, Honeywell, Charlotte, North Carolina, USA) in 1× PBS-T for 1 h in room temperature (RT). The samples were washed four times with 1× PBS-T for 15 min, and then incubated with 10 µg/mL Proteinase K (03115879001, Roche, Basel, Switzerland) in 1× PBS-T, followed by two 10-min washes with 2 mg/mL glycine (G8790-100G, Sigma-Aldrich, Saint Louis, Missouri, USA) in 1× PBS-T. After four 15-min washes with 1× PBS-T, the samples were incubated in 4% PFA in 1× PBS for 20 min, followed by three 15-min washes with 1× PBS-T.

Hybridization step and incubation with antibody were conducted in 2 mL tubes to allow the solution to mix evenly during the incubation period. Hybridization was carried out overnight at +65 °C with rocking, using probes for mouse *Shh* and *Col2a1* (46) with a concentration of 1 µg/mL and a volume of 1 mL. After hybridization, samples were washed two times in 50% formamide (EMSURE, 1.09684.1000, Merck, Darmstadt, Germany), 5× saline sodium citrate (SSC) buffer, and 1% sodium dodecyl sulphate (SDS) solution for 30 min and 3 times in 50% formamide and 2× SSC-solution for 30 min. All washes were conducted at +65 °C.

Before antibody incubation, the samples were washed in 1× maleic acid buffer (MABT). Anti-DIG antibody conjugated with HRP (11207733910, Roche, Basel, Switzerland) was diluted 1 in 50 in solution consisting of 2% blocking reagent (11096176001, Roche, Basel, Switzerland) and 1% goat serum (Gibco, 16210-064, Thermo Fisher Scientific, Waltham, Massachusetts, USA) in 1× MABT. Alkaline phosphatase (AP)–conjugated anti-DIG antibody (11093274910, Roche, Basel, Switzerland) was diluted 1 in 2,000. Used volume of antibody solution was 1 mL. After addition of the antibody, the samples were incubated overnight at +4 °C with rocking and then washed with 1× MABT for three times 15 min, three times 20 min, three times 40 min and for 1 h, RT.

To detect *Shh* and *Col2a1* using alkaline phosphatase activity, BM Purple AP substrate (11442074001, Roche, Basel, Switzerland) was added to the samples with AP-conjugated DIG-antibody. The samples were first washed with AP buffer (100 mM Tris pH 9.5, 100 mM NaCl, 50 mM $MgCl_2$, 0.1 % Tween20) for 10 min and 20 min at RT before adding the substrate. After substrate addition, the samples were incubated and protected from light until strong signal was detected (1 to 4 h RT with *Col2a1* mouse embryos, 15 to 18 h in +4 °C with *Shh* in mouse embryonic lower jaws). After washing the samples with 1× PBS for 3 × 10 min, the samples were fixed with 4% PFA in 1× PBS overnight. The next day, the samples were transferred to 1× PBS for bright-field imaging.

HRP–based detection was carried out using EnzMet General HRP Detection Kit (6010-15 mL, Nanoprobes, Yaphank, New York, USA) according to the manufacturer's protocol. Before detection, samples were transferred from 1× MABT to 1:1 solution of 1× MABT and 100 mM sodium citrate buffer, pH 7 for 5 min, and then washed with sodium citrate buffer for 3 × 15 min.

Equal volumes of solutions A, B, and C of the EnzMet General HRP Detection Kit were added on each sample with anti-DIG antibody conjugated with HRP. Fifteen-minute incubation was conducted in between each addition of detection solution. After addition of solution C, detection solution was continuously mixed and regularly monitored under a light microscope until strong signal was observed and/or first signs of silver precipitate in solution started to emerge (*Col2a1* samples 1 to 7 min, *Shh* samples, 4 to 10 min). After HRP-based detection, the samples were transferred to 1% sodium thiosulfate (217247-25G, Sigma-Aldrich, Saint Louis, Missouri, USA) in deionized water and stored overnight in +4 °C before bright-field imaging and gold enhancement. In the cases where samples were imaged with µCT before proceeding with gold enhancement (*SI Appendix*, Fig. S3*A*), samples were gradually dehydrated to 70% EtOH after bright-field imaging.

Gold Enhancement. Depending on whether the sample was imaged with µCT before gold enhancement, samples were either directly transferred from 1% sodium thiosulfate to 1× PBS (not µCT imaged, Figs. 2–4) or gradually rehydrated from 70% EtOH to 1× PBS (µCT imaged, *SI Appendix*, Fig. S3*A*). The samples were first washed with 1× PBS for 15 min and then transferred to 50 mM glycine in 1× PBS for 15 min, RT. Before reaction initiation, the samples were rinsed in deionized water with 0.1% Tween20 for 15 min, RT. Reaction development was performed following the protocol provided by the manufacturer with small modifications. Equal amounts of solutions A (enhancer) and B (activator) of the kit (GoldEnhance for LM, 2112-28ML, Nanoprobes, Yaphank, New York, USA) were mixed and left to incubate for 10 min before addition of solutions C (initiator), D (buffer), and 0.1% Tween20. Reagent mixture with Tween20 was immediately added to the samples, continually mixed, and monitored regularly under a microscope until signal was as strong as possible without any precipitate in the solution, varying from 2.5 min to 10 min. After detection, the samples were rinsed in deionized water with 0.1% Tween20 for 5 min until fixing with 1% sodium thiosulfate in deionized water with a minimum of 15 min to overnight, RT. To test whether gold enhancement could provide additional means to modulate the signal strength in µCT, the procedure was repeated on lower jaw samples after µCT imaging of first gold enhancement signal.

Vibratome Sectioning. To verify that detection components are capable of penetrating to the region of primary enamel knot, jaw specimens underwent silver deposition and gold enhancement was casted in 6% low-melting point agarose (TopVision, R0801, Thermo Fisher Scientific, Waltham, Massachusetts, USA) in 1× PBS and sectioned to 100 µm sections with vibratome (Microm). The sections were collected in a 6-well plate in 1× PBS and imaged over glass slides mounted in aqueous mounting medium (Shandon Immumount, 9990402, Thermo Fisher Scientific, Waltham, Massachusetts, USA). Vibratome sections were imaged using Zeiss Imager M2 AX10 with AxioCam HRc camera, EC Plan NEOFLUAR 10× objective, and Zeiss Zen2 Pro blue edition software. Images were oriented, cropped, and brightness and contrast were adjusted using ImageJ software (Fiji) (48).

Light Microscopy Imaging. Bright-field images of whole-mount samples were taken using Zeiss Lumar V12 stereomicroscope, AxiocamICc1 camera, Zeiss Zen 2012 blue edition software, and Apolumar S 1.2× objective with magnification of 25× and 12×. Samples were transferred to 1× PBS and set on 4% low-melting point agarose plate to position them. To obtain in-focus images of whole sample, multidimensional acquisition (Z-stack) was used with individually optimized focus plane distance and number of focus planes. Extended depth of focus was achieved using highest alignment of "wavelets"- function in Zeiss Zen 2012 blue edition. Images were cropped, and brightness and contrast were adjusted using ImageJ software (Fiji). After bright-field imaging, samples were gradually dehydrated to 70% EtOH for µCT imaging.

µCT Imaging. X-ray imaging was conducted in 70% EtOH using Bruker SKYSCAN 1272 µCT device in X-ray laboratory in the Department of Physics, University of Helsinki. For tomographic imaging of the overall morphology of whole-mouse

embryos with a voxel size of 3 µm, we used a 0.5-mm aluminum filter, source voltage/current of 70 kV/142 µA, rotation step of 0.1°, and frame averaging of 4. Scanning resulted in 1922 projections over 180° with exposure time of 3,038 ms. Total imaging time was approximately 9 h. The samples were stored in 70% EtOH at + 4 °C until in situ hybridization.

µCT imaging after in situ hybridization was conducted for lower jaws in 70% EtOH using the following settings: 1 µm voxel size, no filter, source voltage/current of 30 kV/212 µA, rotation step 0.1°, frame averaging 5. Scanning resulted in 1877 projections over 180° with exposure time of 1,410 ms. Total imaging time was approximately 4.5 h. For gold enhancement of embryonic lower jaws, a voxel size of 3 µm was used with a 0.25-mm aluminum filter, source voltage/current of 60 kV/166 µA, rotation step of 0.1°, and frame averaging of 5. Scanning resulted in 1922 projections over 180° with exposure time of 1,060 ms. Total imaging time was approximately 4 h. For µCT imaging of gold-enhanced embryos, we used a 3-µm voxel size, 0.25 mm aluminum filter, source voltage/current of 60 kV/166 µA, rotation step of 0.1°, and frame averaging of 4. Scanning resulted in 1992 projections over 180° with exposure time of 2,269 ms. Total imaging time was approximately 7 h.

Reconstruction and Postprocessing. Reconstruction of the µCT data was conducted with nRecon software (1.7.4.2) with misalignment compensation and ring artifact correction optimized separately for each dataset. Regions of interest were reconstructed as 16-bit tiff stacks that were reoriented and cropped in ImageJ (Fiji) before volume rendering and segmentation in Avizo.

Segmentation. Segmentation of expression regions was conducted in Avizo (rel 9.0.1) by first excluding 20% of the darkest pixels in the reconstruction (jaw) and 25% of the darkest pixels in the reconstruction (whole embryo) by using Thresholding tool available in Avizo Segmentation view and then by manually excluding pixels with Brush tool in Segmentation view. Pixels were excluded from expression regions based on evaluation where light microscopy data from chromogenic in situ hybridization, silver in situ hybridization, and gold enhancement were considered together with the location of the signal. In other words, high-intensity pixels on the surface of the specimen and in inconsistent locations throughout detections were considered background and therefore excluded. Extracted volume of expression region was derived by assigning a value of 1 for the segmented voxels and a value of 0 for the voxels remaining outside the signal region in the reconstruction volume using the Arithmetic tool in Avizo. Volume rendering and segmentation images were generated with Avizo using Snapshot tool as 16-bit tiffs. Images were cropped and oriented, and brightness and contrast were adjusted in ImageJ (Fiji).

Data, Materials, and Software Availability. The data supporting the findings of this study are available within the article and its *SI Appendix*. Raw data images and 3D reconstructions are available from the corresponding authors upon a reasonable request.

ACKNOWLEDGMENTS. We thank J. Ollonen and members of the Center of Excellence in Experimental and Computational Developmental Biology for advice and discussions. We thank O. Hallikas, T. Rajala, K. Väänänen, and L. Milocco for commenting the manuscript. We thank A. Viherä, M. Mäkinen, and R. Savolainen for technical assistance. This study was supported by the Academy of Finland and Sigrid Jusélius Foundation (J.J.), Doctoral Programme in Integrated Life Sciences, University of Helsinki (V.V.) and Doctoral Programme in Biomedicine, University of Helsinki (M.M.C.). This work used services of the Helsinki University X-ray Micro-CT Laboratory, funded also by Helsinki Institute of Life Science under HAIP (Helsinki In Vivo Animal Imaging Platform).

Author affiliations: [a]Institute of Biotechnology, University of Helsinki, Helsinki FI-00014, Finland; [b]Department of Physics, University of Helsinki, Helsinki FI-00014, Finland; and [c]Department of Geosciences and Geography, University of Helsinki, Helsinki FI-00014, Finland

1. R. Mizutani, Y. Suzuki, X-ray microtomography in biology. *Micron* **43**, 104–115 (2012).
2. S. D. Rawson, J. Maksimcuka, P. J. Withers, S. H. Cartmell, X-ray computed tomography in life sciences. *BMC Biol.* **18**, 21 (2020).
3. A. M. Zysk *et al.*, Nondestructive volumetric imaging of tissue microstructure with benchtop x-ray phase-contrast tomography and critical point drying. *Biomed. Opt. Express* **3**, 1924–1932 (2012).
4. E. Pauwels, D. Van Loo, P. Cornillie, L. Brabant, L. Van Hoorebeke, An exploratory study of contrast agents for soft tissue visualization by means of high resolution X-ray computed tomography imaging. *J. Microsc.* **250**, 21–31 (2013).
5. S. de Bournonville, S. Vangrunderbeeck, G. Kerckhofs, Contrast-enhanced microCT for virtual 3D anatomical pathology of biological tissues: A literature review. *Contrast Media Mol. Imaging* **2019**, 8617406 (2019).
6. B. D. Metscher, MicroCT for developmental biology: A versatile tool for high-contrast 3D imaging at histological resolutions. *Dev. Dyn.* **238**, 632–640 (2009).
7. B. D. Metscher, Micro CT for comparative morphology: Simple staining methods allow high-contrast 3D imaging of diverse non-mineralized animal tissues. *BMC Physiol.* **9**, 11 (2009).
8. M. Busse *et al.*, Three-dimensional virtual histology enabled through cytoplasm-specific X-ray stain for microscopic and nanoscopic computed tomography. *Proc. Natl. Acad. Sci. U.S.A.* **115**, 2293–2298 (2018).
9. M. Müller *et al.*, Nucleus-specific X-ray stain for 3D virtual histology. *Sci. Rep.* **8**, 17855 (2018).
10. B. Metscher, A simple nuclear contrast staining method for microCT-based 3D histology using lead(II) acetate. *J. Anat.* **238**, 1036–1041 (2021).
11. M. T. Raj *et al.*, Technique: Imaging earliest tooth development in 3D using a silver-based tissue contrast agent. *Anat. Rec.* **297**, 222–233 (2014).
12. M. J. Berger *et al.*, XCOM: Photon Cross Section Database (Version 1.5, National Institute of Standards and Technology, Gaithersburg, MD, 2023), Available: http://physics.nist.gov/xcom.
13. M. Hoshi *et al.*, Reciprocal spatiotemporally controlled apoptosis regulates Wolffian Duct Cloaca fusion. *J. Am. Soc. Nephrol.* **29**, 775–783 (2018).
14. A. T. Kuan *et al.*, Dense neuronal reconstruction through X-ray holographic nano-tomography. *Nat. Neurosci.* **23**, 1637–1643 (2020).
15. O. Ermakova *et al.*, Three-dimensional X-ray imaging of β-galactosidase reporter activity by micro-CT: Implication for quantitative analysis of gene expression. *Brain Sci.* **11**, 746 (2021).
16. S. R. Katz *et al.*, Whole-organism 3D quantitative characterization of zebrafish melanin by silver deposition micro-CT. *Elife* **10**, e68920 (2021).
17. B. D. Metscher, G. B. Müller, MicroCT for molecular imaging: Quantitative visualization of complete three-dimensional distributions of gene products in embryonic limbs. *Dev. Dyn.* **240**, 2301–2308 (2011).
18. I. Tamminen *et al.*, A tube-source X-ray microtomography approach for quantitative 3D microscopy of optically challenging cell-cultured samples. *Commun. Biol.* **3**, 548 (2020).
19. R. D. Powell, J. F. Hainfeld, R. N. Eisen, R. R. Tubbs, Enzymatic metallography: A simple new staining method. *Microsc. Microanal.* **8**, 916–917 (2002).
20. R. D. Powell *et al.*, Metallographic in situ hybridization. *Hum. Pathol.* **38**, 1145–1159 (2007).
21. G. Danscher, Autometallography. *Histochemistry* **81**, 331–335 (1984).
22. W. Grizzle, Theory and practice of silver staining in histopathology. *J. Histotechnol.* **19**, 183–195 (1996).
23. J. F. Hainfeld *et al.*, "Gold-based autometallography" in in *Proceedings of the Fifty-Seventh Annual Meeting, Microscopy Society of America*, , G. W. Bailey, W. G. Jerome, S. McKernan, J. F. Mansfield, R. L. Price, Eds. (Springer-Verlag, 1999), pp. 486–487.
24. K. Weipoltshammer, C. Schöfer, Signal enhancement at the electron microscopic level using Nanogold and gold-based autometallography. *Histochem. Cell Biol.* **114**, 489–495 (2000).
25. G. Danscher, G. W. Hacker, L. Grimelius, J. O. R. Nørgaard, Autometallographic silver amplification of colloidal gold. *J. Histotechnol.* **16**, 201–207 (1993).
26. M. Sandberg, E. Vuorio, Localization of types I, II, and III collagen mRNAs in developing human skeletal tissues by in situ hybridization. *J. Cell Biol.* **104**, 1077–1084 (1987).
27. K. S. Cheah, E. T. Lau, P. K. Au, P. P. Tam, Expression of the mouse alpha 1(II) collagen gene is not restricted to cartilage during development. *Development* **111**, 945–953 (1991).
28. L.-J. Ng *et al.*, SOX9 binds DNA, activates transcription, and coexpresses with type II collagen during chondrogenesis in the mouse. *Dev. Biol.* **183**, 108–121 (1997).
29. K. Sakai *et al.*, Stage-and tissue-specific expression of a Col2a1-Cre fusion gene in transgenic mice. *Matrix Biol.* **19**, 761–767 (2001).
30. M. J. Bitgood, A. P. McMahon, Hedgehog and Bmp genes are coexpressed at many diverse sites of cell-cell interaction in the mouse embryo. *Dev. Biol.* **172**, 126–138 (1995).
31. H. R. Dassule, P. Lewis, M. Bei, R. Maas, A. P. McMahon, Sonic hedgehog regulates growth and morphogenesis of the tooth. *Development* **127**, 4775–4785 (2000).
32. O. Hallikas *et al.*, System-level analyses of keystone genes required for mammalian tooth development. *J. Exp. Zool. Part B Mol. Dev. Evol.* **336**, 7–17 (2021).
33. J. Jernvall, P. Kettunen, I. Karavanova, L. B. Martin, I. Thesleff, Evidence for the role of the enamel knot as a control center in mammalian tooth cusp formation: Non-dividing cells express growth stimulating Fgf-4 gene. *Int. J. Dev. Biol.* **38**, 463–469 (1994).
34. A. Vaahtokari, T. Åberg, J. Jernvall, S. Keränen, I. Thesleff, The enamel knot as a signaling center in the developing mouse tooth. *Mech. Dev.* **54**, 39–43 (1996).
35. J. Jernvall, T. Aberg, P. Kettunen, S. Keranen, I. Thesleff, The life history of an embryonic signaling center: BMP-4 induces p21 and is associated with apoptosis in the mouse tooth enamel knot. *Development* **125**, 161–169 (1998).
36. H.-J. Guder, W. Kunz, S. West, "Colorimetric systems" in *Nonradioactive Labeling and Detection of Biomolecules*, C. Kessler, Ed. (Springer, Berlin Heidelberg, 1992), pp. 159–164.
37. A. M. Elagoz *et al.*, Optimization of whole mount RNA multiplexed in situ hybridization chain reaction with immunohistochemistry, clearing and imaging to visualize octopus embryonic neurogenesis. *Front. Physiol.* **13**, 882413 (2022).
38. T. A. Schoborg, S. L. Smith, L. N. Smith, H. D. Morris, N. M. Rusan, Micro-computed tomography as a platform for exploring Drosophila development. *Development* **146**, dev176685 (2019).
39. E. Hafen, M. Levine, R. L. Garber, W. J. Gehring, An improved in situ hybridization method for the detection of cellular RNAs in Drosophila tissue sections and its application for localizing transcripts of the homeotic Antennapedia gene complex. *EMBO J.* **2**, 617–623 (1983).
40. A. Hemmati-Brivanlou *et al.*, Localization of specific mRNAs in Xenopus embryos by whole-mount in situ hybridization. *Development* **110**, 325–30 (1990).

41. S. Schulte-Merker, R. K. Ho, B. G. Herrmann, C. Nusslein-Volhard, The protein product of the zebrafish homologue of the mouse T gene is expressed in nuclei of the germ ring and the notochord of the early embryo. *Development* **116**, 1021–1032 (1992).
42. B. Rosen, R. S. P. Beddington, Whole-mount in situ hybridization in the mouse embryo: Gene expression in three dimensions. *Trends Genet.* **9**, 162–167 (1993).
43. C. Thisse, B. Thisse, High-resolution in situ hybridization to whole-mount zebrafish embryos. *Nat. Protoc.* **3**, 59–69 (2008).
44. H. Acloque, D. G. Wilkinson, M. A. Nieto, "Chapter 9 IN situ hybridization analysis of chick embryos in whole-mount and tissue sections" in *Avian Embryology*, (Academic Press, ed. 2, 2008), pp. 169–185.
45. J. K. S. Yu, L. Z. Holland, Amphioxus whole-mount in situ hybridization. *Cold Spring Harb. Protoc.* **2009**, pdb.prot5286 (2009).
46. M. Metsäranta, D. Toman, B. De Crombrugghe, E. Vuorio, Specific hybridization probes for mouse type I, II, III and IX collagen mRNAs. *Biochim. Biophys. Acta Gene Struct. Expr.* **1089**, 241–243 (1991).
47. D. G. Wilkinson, M. A. Nieto, Detection of messenger RNA by in situ hybridization to tissue sections and whole mounts. *Methods Enzymol.* **225**, 361–373 (1993).
48. J. Schindelin *et al.*, Fiji: An open-source platform for biological-image analysis. *Nat. Methods* **9**, 676–682 (2012).